OPTICA

# Single-shot phase-contrast computed tomography for multi-material samples

Andrea Mazzolani,[1,*] Alberto Astolfo,[1] Alexander Duncalf,[1] Marius Didziokas,[2] Erwin Pauws,[3] Mehran Moazen,[2] Nicholas Francken,[4] Jitse Verstraete,[4] Peter Modregger,[5] Peter R. T. Munro,[1] and Alessandro Olivo[1]

[1]Department of Medical Physics and Biomedical Engineering, University College London, Malet Place, Gower Street, London WC1E 6BT, UK
[2]Department of Mechanical Engineering, University College London, Roberts Engineering Building, Torrington Place, London WC1E 7JE, UK
[3]Developmental Biology and Cancer Research & Teaching Department, UCL Great Ormond Street Institute of Child Health, University College London, London WC1N 1EH, UK
[4]imec-Vision Laboratory, Department of Physics, University of Antwerp, Universiteitsplein 1, 2610 Wilrijk, Belgium
[5]Physics Department, University of Siegen, Walter-Flex-Str. 3, Siegen 57072, Germany
*andrea.mazzolani.18@ucl.ac.uk

Received 27 August 2025; revised 3 June 2026; accepted 11 June 2026; published 22 July 2026

**Edge illumination (EI) is a mask-based X-ray phase-contrast imaging (XPCI) technique that converts small refraction-induced beam deviations into measurable intensity changes, enabling laboratory-compatible imaging with sensitivity beyond conventional absorption contrast. However, quantitative EI computed tomography typically requires multiple exposures per projection and computationally demanding iterative reconstruction, increasing acquisition time and radiation dose. Here, we present a single-shot technique for quantitative EI phase-contrast CT of multi-material samples based on a linear joint reconstruction (LJR) approach. The method uses a single exposure per angle of projection and directly reconstructs the sample's absorption and phase components simultaneously. This is achieved by applying a first-order Taylor expansion to the system's illumination curve, which linearizes the EI imaging model and transforms it into a convex least-squares problem with a unique semi-analytical solution, eliminating the non-convexity that typically leads to local minima in iterative approaches. As a result, the approach is both fast and robust. We demonstrate the method's performance on both simulated and experimental datasets, including multi-material plastic rods and an intact mouse brain inside its native skull. The results show that the proposed technique produces high-quality, quantitatively accurate phase and absorption tomograms that are a close match to those obtained with the standard EI method while considerably reducing data acquisition and computational time. This development enables rapid, reliable XPCI of complex multi-material samples under challenging imaging conditions.**

Published by Optica Publishing Group under the terms of the Creative Commons Attribution 4.0 License. Further distribution of this work must maintain attribution to the author(s) and the published article's title, journal citation, and DOI.

https://doi.org/10.1364/OPTICA.575949

## 1. INTRODUCTION

X-ray phase-contrast imaging (XPCI) improves soft-tissue visualization by capturing not just absorption but also subtle phase shifts and small-angle scattering that occur as X-rays pass through matter. These additional contrast mechanisms are particularly sensitive to variations in tissue structure and composition, making XPCI well-suited to image low-density or weakly absorbing materials that are nearly invisible in conventional X-ray images. XPCI is particularly advantageous in distinguishing objects with similar absorption coefficients [1]. Over the past decades, XPCI has shown broad applicability, from medical imaging [2–6] to materials science [7], biology [8], and beyond.

Edge illumination (EI) is a laboratory-compatible XPCI method originally developed in the late 1990s at the Elettra Light Source in Trieste, Italy [9,10]. EI employs a dual-mask setup. A pre-sample mask (M1) splits the X-ray beam into narrow beamlets, and a detector mask (M2) in front of the detector, aligned with the pixels' centers, selects specific portions of each beamlet. By partially blocking each beamlet, M2 makes the detected intensity sensitive to beam deflections caused by the sample (i.e., X-ray refraction, which occurs at an angle proportional to the first derivative of the phase shift induced by the object). In conventional EI systems, multiple acquisitions at different relative mask positions are performed for each projection angle (e.g., by shifting M1 in small steps) to measure the so-called illumination curve (IC) for each detector pixel [11,12]. The IC is a bell-shaped intensity profile that encodes the sample's absorption as an overall reduction in the integrated intensity (i.e., the area) and phase-induced refraction as a lateral shift of the curve [13]. Three contrast channels are retrieved—absorption, refraction, and dark-field [12]—by comparing the IC acquired with the sample to the corresponding

flat-field IC obtained without the sample. This retrieval is typically performed by fitting a Gaussian function to the signals with and without the sample, whose estimated parameters directly give information about the three channels. After performing this contrast extraction for every projection angle, separate sinograms for each channel are obtained, and tomographic reconstruction (e.g., filtered backprojection) is applied to each to yield volumetric images.

In summary, the conventional EI workflow proceeds in three distinct stages: first, multiple frames are acquired at different mask positions; second, an explicit phase retrieval step is performed; and finally, the retrieved projections undergo standard tomographic reconstruction. While effective, the multi-exposure approach increases acquisition time and dose. From now on, we will refer to the standard EI method with multiple acquired points on the IC as "EI." To address these limitations, there has been growing interest in single-shot methods. Diemoz *et al.* [14,15] adapted the work of Paganin *et al.* [16] to EI, developing a single-shot EI (SS-EI) reconstruction applicable to general imaging geometries, which operates under the assumption that the ratio between phase shift and absorption ($=\delta/\beta$) is uniform across the entire sample [14,15]. This approximation works well for homogeneous samples or for those composed of materials with similar characteristics. However, it fails to quantitatively retrieve multi-materials presenting different $\gamma$ values. To address this issue, Zamir *et al.* [17] proposed an advanced reconstruction method designed to handle samples composed of multiple, distinct materials, adopting an approach conceptually similar to that introduced earlier by Beltran *et al.* [18,19]. Despite this improvement, the technique depends on prior knowledge of the constituent materials and assumes that each material is surrounded by a single background, with the outer material varying smoothly in thickness along the X-ray propagation. Similar efforts applied to other X-ray phase-contrast techniques include uniqueness analyses and regularized non-linear inversion methods for propagation-based phase-contrast imaging, including single-measurement phase retrieval and simultaneous phase/amplitude recovery without homogeneity constraints [20,21]. In grating-based phase-contrast CT, related single-shot direct reconstruction approaches have also been proposed to recover attenuation, refractive-index, and dark-field information from a single measurement per projection angle [22].

In the last decade, a new single-shot EI approach to quantitatively retrieve $\delta$ and $\beta$ has been developed that eliminates the need for prior assumptions about material properties. In particular, a fully general joint reconstruction (JR) framework was introduced by Chen *et al.* [23–25], in which phase retrieval and tomographic inversion are performed in one unified step.

In the JR framework, absorption and phase distributions are simultaneously estimated by fitting the EI forward model to the measured projection data. Instead of separating phase retrieval and tomographic reconstruction into distinct steps, JR algorithms jointly refine the $\beta$ and $\delta$ maps so that the predicted intensities align with the experimental measurements. This integrated approach accommodates complex, multi-material compositions without assuming a fixed $\gamma$ ratio and naturally incorporates both contrast mechanisms into a single inversion process. Optimization is typically performed using iterative gradient-descent-based methods. More recently, a gradient-descent scheme incorporating Barzilai–Borwein steps has been proposed, which also includes scatter reconstructions [25].

Two key problems of existing non-linear JR methods are that the multiple iterations needed for convergence lead to long processing times and, more importantly, that the objective function is inherently non-convex [23,26]. This means that the solution is not guaranteed to be unique or to correspond to the global minimum since the algorithm may converge to a local minimum depending on initialization and regularization. This non-convexity arises from the exponential absorption term and the phase-induced shift within the illumination curve.

Consequently, the final estimates of $\delta$ and $\beta$ may deviate from the true values, particularly in the absence of careful initialization or regularization. Successful reconstructions of random phantoms have proved that using zero-valued initial guesses can mitigate the impact of non-convexity [26].

In this paper, we propose a new JR method for EI that, unlike previous approaches, is semi-analytical, fast, and robust. The key innovation is a unique solution based on the first-order Taylor expansion of the logarithm of the illumination curve, which yields a linear forward model relating the sample's properties to the measured intensities. This linearization effectively transforms the minimization problem related to JR into a convex problem with a unique solution, eliminating issues of non-convexity and ambiguous minima. For this reason, we denote the new method as the linear joint reconstruction method (LJR). As well as for standard JR methods, LJR does not require Gaussian fitting of the IC; instead, the solution can be obtained by applying a linear regression to an *ad hoc* approximate version of the raw projections.

## 2. LINEAR JOINT RECONSTRUCTION METHOD

In EI systems, the retrieved quantities are $I_\beta(x_s;\theta) := \int_{z_1}^{z_2} \beta(x_s, z;\theta)\mathrm{d}z$ and $I_\delta(x_s;\theta) = \int_{z_1}^{z_2} \delta(x_s, z;\theta)\,\mathrm{d}z$, along with the scattering signal [12,27], which is only analyzed in this paper to quantify its impact on the model and not explicitly retrieved in the reconstruction.

$\theta$ is the projection angle, $M$ is the magnification of the system and the variable $x_s = \frac{x}{M}$ denotes the demagnified transverse coordinate in the object domain, and $x$ is the coordinate at the detector. By considering a sample composed of $N_m$ materials, equivalent to assuming a stepwise approximation of both the $\delta$ and $\beta$ maps, we can rewrite these integrals as

$$I_\beta(x_s;\theta) = \sum_{j=1}^{N_m} \beta_j\, T_j(x_s;\theta), \tag{1a}$$

$$I_\delta(x_s;\theta) = \sum_{j=1}^{N_m} \delta_j\, T_j(x_s;\theta), \tag{1b}$$

where the functions $T_j$ represent the thickness of the $j$th material as a function of the sample coordinate $x_s$ and angle $\theta$. We denote the illumination curve function (IC) without the sample as $\mathcal{C}(t)$, so that the projection acquired without a sample is $P_f(t) = N_p\mathcal{C}(t)$, where $N_p$ is a scaling factor modeling the number of photons that reach the detector. The effect of the scattering due to the sample on the X-ray beamlets is a broadening on $\mathcal{C}(t)$, which we model via convolution with a Gaussian distribution $f_{sc}(t;\sigma_{sc}) = \frac{1}{\sqrt{2\pi}\sigma_{sc}} \exp\left(-\frac{t^2}{2\sigma_{sc}^2}\right)$, and the broadened IC: $\mathcal{C}_{\sigma_{sc}}(t) = \mathcal{C}(t) * f_{sc}(t;\sigma_{sc})$. The intensity recorded by a single detector pixel $x_s$ at projection angle $\theta$ and mask displacement $t$ can

be described by the forward model [12,28,29]:

$$P_s(x_s;\,t,\,\theta) = N_p e^{-2k_0 I_\beta(x_s;\theta)} \mathcal{C}_{\sigma_{sc}}\left(t - \frac{z_{od}}{M}\frac{\partial}{\partial x_s} I_\delta(x_s;\,\theta)\right), \tag{2}$$

where $k_0$ is the central wave number, $z_{od}$ is the distance between the sample and the detector, and $P_s$ is the raw projection acquired by the detector. As stated above, the dark-field signal is not retrieved by the proposed model; therefore, we assume scattering effects to be negligible and approximate $\mathcal{C}_{\sigma_{sc}}(t) \approx \mathcal{C}(t)$. Following the approach of Diemoz *et al.* [14], we apply a first-order Taylor expansion to Eq. (2) with center "$t$." Introducing the parameter $T$ defined as $T = t - \frac{z_{od}}{M}\frac{\partial}{\partial x_s} I_\delta(x_s;\,\theta)$, we obtain $P_s(x_s;\,t,\,\theta) \approx N_p\, e^{-2k_0 I_\beta(x_s;\theta)}[\mathcal{C}(t) + \mathcal{C}'(t)(T - t)] = N_p\, e^{-2k_0 I_\beta(x_s;\theta)}(\mathcal{C}(t) - \frac{z_{od}}{M}\frac{\partial}{\partial x_s} I_\delta(x_s;\,\theta)\,\mathcal{C}'(t))$, where the superscript $'$ represents the derivative respect to the variable $t$. Subsequently, dividing by $P_f(t)$ and taking the logarithm, we have

$$\mathcal{L}(x_s;\,t,\,\theta) := \log\left(\frac{P_s(x_s;\,t;\,\theta)}{P_f(x_s;\,t)}\right) \tag{3a}$$

$$\approx -2k_0 I_\beta(x_s;\,\theta) + \log\left(1 - J_{EI}\frac{\partial}{\partial x_s} I_\delta(x_s;\,\theta)\right) \tag{3b}$$

$$\approx -2k_0 I_\beta(x_s;\,\theta) - J_{EI}\frac{\partial}{\partial x_s} I_\delta(x_s;\,\theta) \tag{3c}$$

$$= -2k_0 \sum_{j=1}^{N_m} \beta_j\, T_j(x_s;\,\theta) - J_{EI} \sum_{j=1}^{N_m} \delta_j \frac{\partial}{\partial x_s} T_j(x_s;\,\theta), \tag{3d}$$

where $J_{EI} = \frac{z_{od}}{M}\frac{\mathcal{C}'(t)}{\mathcal{C}(t)}$, and Eq. (3c) results from applying the first-order Taylor expansion of the logarithmic term at $x = 0$ to Eq. (3b) $\big(\log(1 + x) \approx x\big)$. The approximation introduced in Eq. (3c) is valid provided that the term $J_{EI}\frac{\partial}{\partial x_s} I_\delta(x_s;\,\theta)$ remains *small* in magnitude. This requirement is essentially the same assumption underlying the Diemoz *et al.* approximation, although here it is applied in a slightly more relaxed form. We quantified the error of both the LJR and Diemoz *et al.* approaches assuming a Gaussian illumination curve $\mathcal{C}(t) = \exp\left(-\frac{t^2}{2\sigma^2}\right)$. Under this assumption, and assuming noise-free conditions, no cross-talk, and no scattering, both approaches reproduce the $I_\beta$ term of $\mathcal{L}(x_s;\,t,\,\theta)$ exactly, so the only approximation error appears in the $I_\delta$ contribution. For LJR, the leading error is always *second-order* in the small parameter, whereas for the Diemoz *et al.* approximation, it is likewise second-order under typical conditions but improves to *third-order* when the illumination is sampled at the "optimal" point $t_0 = \sigma$ (more details of this analysis are provided in Section 1 of Supplement 1). We emphasize that this analysis is not intended to judge which method is superior. LJR is specifically designed to yield quantitative refractive-index maps in multi-material samples, capabilities that lie outside the remit of the Diemoz *et al.* approximation. The comparison is presented solely to demonstrate that the small-signal assumption underpinning LJR is sound, with an accuracy that differs from the optimal Diemoz *et al.* case by just one order in the already small expansion parameter. In Section 4, we will quantify the error committed by neglecting the scattering, which will help to assess the robustness and accuracy of the presented model under such an assumption. Given that the term in Eq. (3d) is linear in $\beta_j$ and $\delta_j$, we can retrieve analytical estimations of these parameters by solving the following least-squares error minimization problem:

$$E\left(\boldsymbol{\beta}^x, \boldsymbol{\delta}^x\right) = \sum_{i=1}^{N_\theta} \int_{\mathbb{R}} \Bigg| \mathcal{L}\left(x_s;\,t,\,\theta_i\right) + 2k_0 \sum_{j=1}^{N_m} \beta_j^x\, T_j\left(x_s;\,\theta_i\right) + J_{EI} \sum_{j=1}^{N_m} \delta_j^x \frac{\partial}{\partial x_s} T_j\left(x_s;\,\theta_i\right) \Bigg|^2 \mathrm{d}x_s, \tag{4}$$

where $N_\theta$ is the number of angle projections. The integral over $x_s$ is evaluated in practice as a sum over detector pixels. A detailed derivation of the minimization of Eq. (4) and a discussion of well-posedness are provided in Section 2 of Supplement 1.

The optimal values $(\beta_j^{\mathrm{opt}}, \delta_j^{\mathrm{opt}})$ that minimize $E(\beta_j^x, \delta_j^x)$ are given by

$$\boxed{A\hat{x} + b = 0} \Rightarrow \hat{x} = \begin{pmatrix} \beta_1^{\mathrm{opt}} \\ \vdots \\ \beta_{N_m}^{\mathrm{opt}} \\ \delta_1^{\mathrm{opt}} \\ \vdots \\ \delta_{N_m}^{\mathrm{opt}} \end{pmatrix} \Rightarrow \hat{x} = -A^{-1} b,$$

$$A_{hk}, \quad b_h = \text{coeff.} \quad \text{(See table below)}$$

Convergence to the global minimum is guaranteed since the problem is convex. We emphasize that, unlike in some prior

| Case | $A_{hk}$ | $b_h$ |
|---|---|---|
| $h \le N_m,\ k \le N_m$ | $2\,k_0 \sum_{i=1}^{N_\theta} \int_{\mathbb{R}} T_k(x_s;\,\theta_i)\; T_h(x_s;\,\theta_i)\,\mathrm{d}x_s$ | $\sum_{i=1}^{N_\theta} \int_{\mathbb{R}} \mathcal{L}(x_s;\,t,\,\theta_i)\; T_h(x_s;\,\theta_i)\,\mathrm{d}x_s$ |
| $h \le N_m,\ k > N_m$ | $J_{EI} \sum_{i=1}^{N_\theta} \int_{\mathbb{R}} T_h(x_s;\,\theta_i)\; T_k'(x_s;\,\theta_i)\,\mathrm{d}x_s$ | |
| $h > N_m,\ k \le N_m$ | $2\,k_0 \sum_{i=1}^{N_\theta} \int_{\mathbb{R}} T_h'(x_s;\,\theta_i)\; T_k(x_s;\,\theta_i)\,\mathrm{d}x_s$ | $\sum_{i=1}^{N_\theta} \int_{\mathbb{R}} \mathcal{L}(x_s;\,t,\,\theta_i)\; T_h'(x_s;\,\theta_i)\,\mathrm{d}x_s$ |
| $h > N_m,\ k > N_m$ | $J_{EI} \sum_{i=1}^{N_\theta} \int_{\mathbb{R}} T_h'(x_s;\,\theta_i)\; T_k'(x_s;\,\theta_i)\,\mathrm{d}x_s$ | |

approaches, we do not assume a proportionality between the phase and absorption distributions—the algorithm retrieves both $\delta(x, y)$ and $\beta(x, y)$ independently, which is essential for truly multi-material imaging. In order to create the matrix $A_{h,k}$ and the vector $b_h$, we need to estimate the terms $T_j(x_s; \theta)$.

The first step to estimate $T_j$ is to apply the Diemoz *et al.* filter [14] to the raw projections, so as to *qualitatively* highlight different materials. Let us call $\mathcal{L}_D$ the result of this processing stage. Its inverse Radon transform $\mathcal{S}_D$ is a good candidate to emphasize different materials within the sample. It is worth noting that, in the case of a single material sample, $\mathcal{S}_D$ *quantitatively* reconstructs the $\delta$ map and $\beta$ map, the latter obtained by multiplying the $\delta$ map by the $\gamma$ parameter. Then, we choose the number of distinct materials $N_m$, corresponding to $N_m$ intensity bands between the minimum and maximum of $\mathcal{S}_D$. The next step is the definition of $N_m$ boolean matrices $B_j$ containing *ones* only for pixels whose intensity values belong to the $j$th band. The boolean matrices $B_j$ represent a normalized version of the inverse Radon transform of *exclusively* the $j$th material. Then, $T_j$ corresponds to the radon transform of $B_j$.

## 3. VALIDATION ON SIMULATED AND EXPERIMENTAL DATA

We validated the proposed method through both simulated and experimental studies, from which we present three representative case studies. First, a simulated multi-material phantom consisting of plastic rods was used to assess quantitative accuracy under ideal conditions. Second, an experimental scan of a rod phantom containing two materials with different refractive indices demonstrated the method's performance on real data. Finally, an intact mouse skull with the brain was used to challenge the method on a complex biological sample involving materials with very different properties, such as bone and soft tissue. In all cases, the results obtained with the proposed method were compared to reference images reconstructed using the conventional (multi-shot) EI approach, which involves multiple mask positions and standard retrieval. Additionally, some experimental data were compared with reconstructions performed with the Barzilai–Borwein step-based joint reconstruction method with split gradient-descent [25], hereafter referred to simply as JR.

### A. Simulation: Multi-Material Rod Phantom

As a first validation step, we designed a numerical phantom consisting of two intersecting cylindrical rods. The intersection created three distinct regions, to which we assigned different values of $\delta$ and $\beta$ (see Fig. 1), allowing us to assess the method's ability to accurately recover multiple material properties in a controlled setting.

The simulation was carried out using the EI simulator developed by Vittoria *et al.* [30]. A polychromatic X-ray spectrum ranging from 21 to 36 keV was used, and the extended X-ray source was modeled with a Gaussian intensity profile having a focal spot full width at half-maximum (FWHM) of 70 μm. The source-to-$M_2$ and source-to- $M_1$ distances were set to 0.86 and 0.68 m, respectively, resulting in $M \approx 1.26$. The sample was positioned at the same longitudinal location as $M_1$ for simplicity, thereby avoiding the simulation of an additional free-space propagation stage, which was found to have a negligible impact on the results under the conditions considered. The aperture sizes of $M_1$ and $M_2$ were set to 10 and 17 μm, respectively. The detector pixel size was set to 50 μm. To simulate a skipped detector mask configuration, the period $\mathcal{P}_2$ of $M_2$ was set to twice the pixel size and $\mathcal{P}_1 = \frac{\mathcal{P}_2}{M}$. With this setup, every other detector pixel was obscured, resulting in an alternating pattern of active and inactive pixels. The two simulated rods were placed with a center-to-center distance of 3.9 mm.

The smaller rod had the refractive index of a polytetrafluoroethylene (PTFE) with a density of 2.15 $\frac{g}{cm^3}$ and a radius of 3.6 mm. Its effective refractive index decrement and absorption index were set to $\delta_{\text{eff}} = 6.98 \times 10^{-7}$ and $\beta_{\text{eff}} = 4.61 \times 10^{-10}$, respectively. The larger rod was modeled as low-density polyethylene (LDPE) with a density of 0.925 $\frac{g}{cm^3}$ and a radius of 4.3 mm. It was assigned $\delta_{\text{eff}} = 3.56 \times 10^{-7}$ and $\beta_{\text{eff}} = 1.06 \times 10^{-10}$. In the intersection region, both $\delta$ and $\beta$ were set to the sum of the corresponding values from the two rods. The X-ray source spectrum was set to match that of the Rigaku MicroMax-007HF with a molybdenum anode and a focal spot size of 70 μm × 100 μm (horizontal × vertical), where the horizontal direction corresponds to the direction of phase sensitivity. For each region with a uniform refractive index, the values $\delta_{\text{eff}}$ and $\beta_{\text{eff}}$ were computed as the weighted averages of the energy-dependent $\delta$ and $\beta$, respectively, over the source spectrum. To enhance image detail, a "dithering" approach was employed: for each projection angle and each illumination curve position, three acquisitions were simulated while shifting the sample in sub-pixel steps.

We simulated raw intensity projections of the phantom over a full 360° rotation. For the reference dataset, we simulated a conventional EI scan with 15 mask positions per projection, covering the full illumination curve for each pixel. These projections were processed by fitting Gaussian functions to extract absorption and refraction sinograms, which were then reconstructed using filtered backprojection to obtain separate $\beta$ and $\delta$ tomograms (referred to as the "standard EI" result). For the single-shot test, only a *single* mask position per projection was simulated, corresponding to 60% of the maximum of the illumination curve. Binary masks $B_j$ were taken directly from the simulated phantom geometry defining the materials; an automated masking approach is introduced in Section 3.D.

Figure 1 shows a representative slice for three cases: the simulated ground-truth maps used as reference [panels (a1) and (a2)], and the corresponding reconstructions obtained with the standard EI approach [panels (b1) and (b2)] and with the proposed LJR method [panels (c1) and (c2)].

The slices were reconstructed by maintaining the same pixel size of the projections obtained after recombining the three dithered images, corresponding to a pixel size of $\frac{\mathcal{P}_1}{3} \approx 26$ μm. All images shown in Fig. 1 were previously cropped around the objects, and the final size of each image is 481 × 611.

The LJR reconstruction appears visually very similar to the standard multi-shot EI result. All three regions are clearly distinguishable, and the relative phase shifts align well with the material properties given as input to the simulation. To better quantify the accuracy for both $\beta$ and $\delta$, line profiles across the rods are shown in plots (d1) and (d2), respectively. Panels (e1), (f1), (e2), and (f2) present the error maps for both EI and LJR reconstructions of the $\delta$ and $\beta$ channels. These maps highlight the regions where each method deviates from the ground truth and provide a direct visual comparison of their accuracy. Under ideal conditions, this simulation confirms that the LJR model can accurately recover both contrast channels in a multi-material object. Notably, the LJR method succeeds in reconstructing each

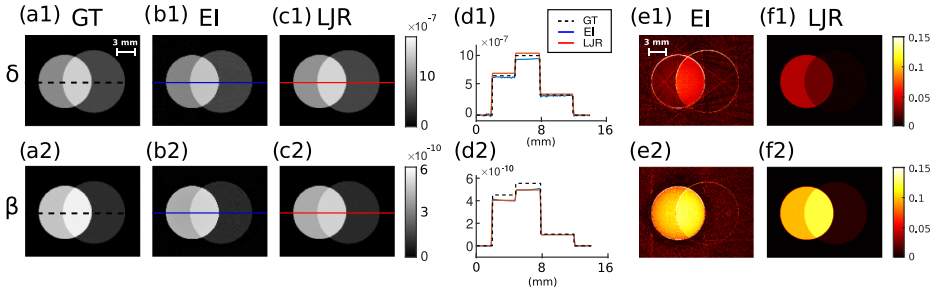


**Fig. 1.** Simulation of a multi-material rod phantom. Top row: reconstructed $\delta$-map slices using the ground truth (a1), the standard EI method with 15 IC sampling points per projection (b1), and the proposed LJR method, which is inherently single-shot (c1). (d1) Line profile comparison along the central horizontal line crossing the intersection region in (a1)–(c1), with the reference $\delta_{\text{eff}}$ values overlaid for validation. (e1) and (f1) Magnitude of the difference between each reconstruction and the ground truth, normalized by the maximum value of the ground truth. Bottom row: same set of reconstructions, line profiles, and error analyses as the top row, but for the $\beta$ maps instead of the $\delta$ maps.

material's properties without cross-contamination between phase and absorption signals—an important feature when dealing with complex samples.

A non-negligible discrepancy can be observed between the reconstructions and the expected effective values, especially for the $\beta_{\text{eff}}$ [panels (d2)–(f2)]. This deviation arises because both the EI and JR methods assume a monochromatic forward model. While the definitions of $\delta_{\text{eff}}$ and $\beta_{\text{eff}}$ can be used as first-order approximations in a polychromatic simulation, the unavoidable beam hardening still introduces reconstruction errors. Quantitatively, the average relative errors of the EI and LJR $\delta$ reconstructions with respect to the ground truth (GT) are 4.7% and 3.7%, respectively, whereas the corresponding errors for $\beta$ are 10.7% and 10.9%. Comparing the two reconstruction methods directly, the average relative differences are 7.2% for $\delta$ and only 0.6% for $\beta$.

### B. Experimental Setup and Acquisition Parameters

This section describes the experimental imaging system, acquisition settings, and preprocessing procedures used for the experimental datasets acquired at the Advanced X-Ray Imaging (AXIm) Labs at University College London.

The source-to-$M_1$ and source-to-$M_2$ distances, as well as the aperture sizes for masks $M_1$ and $M_2$, matched those used in the simulations. All samples were placed inside cylindrical plastic containers (1.6 cm in diameter and 5 cm in height), which correspond to the largest annular structures visible in all the reconstructed images. The distance between the sample center and $M_1$ was set to 20 mm. A Hamamatsu CMOS Flat Panel Sensor (C9732DK) with a 50 µm pixel size and a direct-deposited CsI scintillator was used for detection. The X-ray source was a Rigaku MicroMax-007HF with a molybdenum anode and an approximate focal spot size of 70 µm × 100 µm (horizontal × vertical), where the horizontal direction corresponds to the direction of phase sensitivity. The system's point spread function (PSF) was estimated to distribute approximately 40%, 12%, and 2% of the signal into the first, second, and third adjacent pixels, respectively. The X-ray tube was operated at 40 kV and 30 mA, and the exposure time per frame was 1.2 s, with no frame averaging applied. We also applied our recently proposed cross-talk deconvolution algorithm based on circulant matrix deconvolution [31] to the retrieved projections. This method improves both image quality and quantitative accuracy and proved particularly effective in enhancing the visualization of soft tissue structures in the brain.

### C. Analysis of a Multi-Material Plastic Rods Phantom

We applied EI, JR, and LJR methods to a CT scan of a phantom containing three objects: a low-density polyethylene (LDPE) rod with a diameter of 6.65 mm, a polytetrafluoroethylene (PTFE) rod with a diameter of 4.15 mm, and a plastic straw with a diameter of 4.8 mm. The reconstructed slices are shown in Fig. 2. Each scan employed 16 dithering steps to improve spatial resolution. For this experiment, four positions along the illumination curve were used, corresponding to 13%, 35%, and 100% of its maximum, and 45% on the opposite side of the illumination curve peak. A total of 720 projections were acquired at equally spaced angles over a 360-deg range. Analogously to the simulations, the slices were reconstructed using the same pixel size as the projections obtained after recombining the 16 dithered images, corresponding to $\frac{\mathcal{P}_1}{16} \approx 4.9$ µm. All images shown in Fig. 2 were previously cropped around the objects, and the final size of each image is 3801 × 3801 pixels. For the LJR method, we used only the single-shot data acquired at the mask position corresponding to 35% of the illumination curve maximum for each projection. For JR, we obtained the most stable and accurate reconstructions by cyclically selecting, for each projection angle, one of the four acquired mask positions; the results presented here correspond to this heuristically determined "optimal" configuration. A drop of distilled water, trapped between the straw and the LDPE rod from previous usage, is visible in the central region of images (a2)–(c2). For this case, since the components of the phantom were known in advance, we used this a priori knowledge to manually define the five binary images $B_j$ used as input to the LJR algorithm. A more general, automated version based on pixel intensity thresholds rather than prior knowledge will be presented in Section 3.D, where $\delta$ and $\beta$ maps are quantitatively retrieved from the mouse skull sample. The top row shows the reconstructed $\delta$ maps, while the bottom row displays the corresponding $\beta$ maps. Reconstructions obtained with the standard EI, LJR, and JR methods are shown in the first, second, and third columns, respectively. The blue and green lines in plot (a1) indicate the positions of the line profiles shown in plots (d1)–(e1) and (d2)–(e2), respectively. Black lines represent the effective refractive index values averaged over the spectrum ($\delta_{\text{eff}}$ and $\beta_{\text{eff}}$) and do not include the plastic container nor the straw. Due to the high noise level in the EI $\beta$ reconstruction, the images in panels (a2)–(c2) were spatially averaged over 5 × 5 pixels. To improve the visibility of the line profiles, the EI and JR reconstructions shown in panels (d2) and (e2) were spatially averaged over

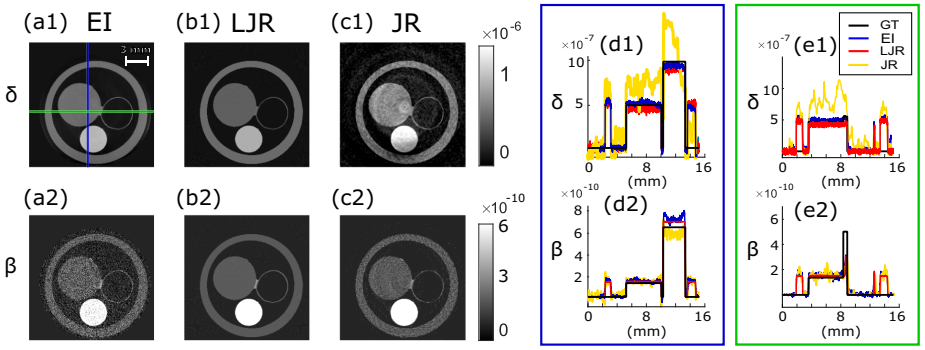


**Fig. 2.** Multimaterial phantom. Top row: reconstructed $\delta$-map slices using the standard EI method (a1), the proposed LJR method (b1), and JR (c1). (d1) and (e1) Line profile comparison along the central vertical line and horizontal line, which have been drawn in the panel (a1) as a reference. The line values of (a1), (b1), (c1), and the GT ($\delta_{\text{eff}}$) have been colored in blue, red, yellow, and black, respectively. Bottom row: corresponding results for $\beta$, with reconstructions from EI (a2), LJR (b2), and JR (c2), and the related line profile comparison (d2) and (e2).

$35 \times 35$ pixels prior to extracting the line profiles. The results of Fig. 2 demonstrate that the LJR method can quantitatively retrieve both $\delta$ and $\beta$ maps for multi-material samples with an accuracy comparable to that of standard EI and seems to reduce the noise of $\beta$. We ran the JR method for 5000 iterations, achieving a level of accuracy in the $\beta$ reconstruction comparable to that obtained with EI and LJR. The $\delta$ maps were also reconstructed with comparable results; however, the values appeared to be slightly higher than the expected ones and were noticeably noisier than those obtained with EI and LJR. Section 4 of Supplement 1 reports the relative errors for LDPE, PTFE, and water for the three reconstruction methods. The computational time for the complete reconstructions including both $\delta$ and $\beta$ maps was $\approx 13$ min for EI, 40 s for LJR, and approximately 6 h for JR. The LJR method generally includes an additional segmentation step to identify different materials; however, this step was not required for the present sample, resulting in a particularly low computational time for LJR. This point is discussed in more detail in Section 3.D.

### D. Post-Mortem Imaging of a Mouse Head

In this section, we evaluate the performance of the LJR algorithm on a particularly challenging dataset. Imaging soft tissue structures, such as the brain, enclosed within a dense bony shell like the skull, poses significant difficulties for phase-contrast methods, especially when using laboratory-based setups. The strong absorption from bone, combined with steep phase variations at the bone–tissue interface, can introduce artifacts and destabilize the phase retrieval process.

For this experiment, five positions along the illumination curve were used, corresponding to 14%, 58%, 100%, 58%, and 14% of its maximum. A total of 2000 projections were acquired at equally spaced angles over a 360-deg range. The sample was provided by the Pauws lab as part of a UK Home Office Project License (number: PP8161503) under the UK Animals (Scientific Procedures) Act 1986. The animal procedure complied with the ARRIVE guidelines and was performed under the supervision of UCL Biological Services. The specimen is a postnatal day 21 (P21) wild-type (CD-1 strain) mouse. For the LJR method, we used only the single-shot data acquired at the mask position corresponding to 58% of the illumination curve maximum for each projection and applied the reconstruction.

We now describe the construction process for the binary images $B_j$, which are used to define the thickness functions $T_j(x_s;\theta)$. As a first step, we computed the normalized projection $\mathcal{L}_j(x_s;t_0)$ evaluated at $t_0 = 2$ (58% of the illumination curve maximum). We then applied the Diemoz *et al.* filter using a reference value of $\gamma = \frac{3\times10^{-7}}{6\times10^{-10}}$, which represents a reasonable approximation for biological tissues imaged at an average energy of $\approx 20-22$ keV. We emphasize that this choice was not based on a rigorous analysis, as the Diemoz *et al.* filter was not used to retrieve $\beta$ and $\delta$, but solely to enhance the image quality of the CT reconstructed slice from $\mathcal{L}_D$, which is the inverse Radon transform of $\mathcal{L}_D(x_s;t,\theta)$. Accordingly, the reconstructed slice is a linear combination of $\beta$ and $\delta$ [see Eq. (3c)]. Because the $\beta$ term is multiplied by the wavenumber $k$, it dominates in magnitude for most pixels; for clarity, we therefore denote the values of $\mathcal{S}_D$ by $\tilde{\beta}$ hereafter.

The second step defines the binary images (masks) $B_j$. In the absence of a predefined geometry, the $B_j$ is obtained by grouping pixels with similar intensities. We determine the bin edges for $\tilde{\beta}$ by combining a noise-driven lower bound with an adaptive promotion rule that favors a spatially coherent structure. Specifically, let $\Omega_{\text{out}}$ denote a background region in the $\tilde{\beta}$ slice, outside the sample support, where the true $\tilde{\beta}$ is expected to be zero. Because the physical $\beta$ ($\approx \tilde{\beta}$) is non-negative, negative values in $\Omega_{\text{out}}$ are treated as noise. We therefore compute the standard deviation over *positive* entries only, $\sigma_+ = \text{std}\{\tilde{\beta}(p) : p \in \Omega_{\text{out}},\ \tilde{\beta}(p) > 0\}$, where $p$ indexes pixels in the $\tilde{\beta}$ image, and set the noise–soft boundary as $\tilde{\beta}_{\text{ns}} = 2\,\sigma_+$. We then build a dense grid over a broad interval that comfortably contains all relevant values:

$$\mathcal{G}_{\text{fine}} = \{\,\tilde{\beta}^{(k)} : \tilde{\beta}^{(k)} = k\,\Delta\tilde{\beta},\ k = 0, 1, \ldots, 2000\},$$

$$\Delta\tilde{\beta} = 5 \times 10^{-12},$$

so that $\mathcal{G}_{\text{fine}} = [0,\ 10^{-8}]$ with 2001 points. Candidates below the noise bound are discarded:

$$\mathcal{G}_{\text{cand}} = \{\tilde{\beta}^{(k)} \in \mathcal{G}_{\text{fine}} : \tilde{\beta}^{(k)} \geq \tilde{\beta}_{\text{ns}}\}.$$

Starting from $\tilde{\beta}_1 = \tilde{\beta}_{\text{ns}}$, we traverse $\mathcal{G}_{\text{cand}}$ in ascending order and accept a new edge $\tilde{\beta}_{j+1}$ as the *first* candidate $\tilde{\beta}^{(k)} > \tilde{\beta}_j$ that yields a sufficiently large and spatially coherent set of *new* pix-

els. Concretely, we define for each tested candidate the boolean "surplus" mask:

$$B_j^{(k)}(p) = \mathbf{1}\left\{ \tilde{\beta}_j \le \tilde{\beta}(p) < \tilde{\beta}^{(k)} \right\},$$

where $\mathbf{1}\{\cdot\}$ is the indicator function. We accept $\tilde{\beta}^{(k)}$ if $B_j^{(k)}$ contains at least one $5 \times 5$ window with $\geq 75\%$ ones (i.e., $\geq 19$ of 25 pixels); otherwise, we increase $k$ and test the next candidate. Then, we set $\tilde{\beta}_{j+1} = \tilde{\beta}^{(k)}$ and $B_{j+1} = B_j^{(k)}$. The procedure repeats until the upper bound $10^{-8}$ is reached, yielding a data-driven set of coarse edges $\tilde{\beta}_j$. This strategy anchors the noise–soft boundary to measured background fluctuations, explores $\tilde{\beta}$ over a wide interval with fine resolution, and promotes new edges only when they reveal spatially coherent structure, naturally allocating more bins to rapidly varying soft-tissue ranges and fewer to slowly varying hard tissues. To facilitate segmentation, we applied a low-pass filter to $\mathcal{L}$ by zeroing all Fourier components (computed along the pixel rows) above 40% of the maximum frequency. Once the segmentation was defined, however, the minimization problem was solved using the unfiltered $\mathcal{L}$. With this approach, the number of defined binary images $B_j$ for this sample was 47. An additional bin was assigned to the plastic container (the only component with known geometry), giving a total of $N_m = 48$. In Section 4, we show that $\Delta\tilde{\beta} = 5 \times 10^{-12}$ is a robust choice for generic samples. Setting higher values of $\Delta\tilde{\beta}$ (practically reducing the number of $B_j$) could be unsafe, as it produces an overly coarse material basis and may compromise the accuracy of the reconstruction. As in the plastic-rod phantom, we compare reconstructions obtained with the EI and LJR methods. For this experimental dataset, we do not include a comparison with the JR method, as it did not provide satisfactory results: both the $\delta$ and $\beta$ reconstructions were excessively noisy, with particularly poor performance in the gray matter region.

In Fig. 3(a), we show the intensity histogram of the reconstructed slice on a log–log scale: the left tail corresponds to background noise, the central peak to soft tissue (primarily brain), and higher $\tilde{\beta}$ values to hard tissue (bone). The resulting binning is noticeably finer in the soft-tissue region than in the hard-tissue region. In Figs. 3(b) and 3(c), we present the results obtained by averaging the reconstructed $\delta$ and $\beta$ maps over individual bins $B_j$. Each point represents the mean value computed over all pixels belonging to a single bin. The red and blue curves correspond to reconstructions obtained using the EI and LJR methods, respectively. The x axis is displayed on a logarithmic scale, and the points are connected to visualize the trend across bins. Highly dense material regions are represented by only a few pixels, leading to eroded masks and limited statistical support. This, in turn, affects the local accuracy of the LJR and may explain the small fluctuations observed in the retrieved quantities.

### 1. Error Analysis

We also included estimated intervals for the minimum and maximum expected values of $\delta$ and $\beta$ for cortical bone (the densest and hardest bone components), as well as for soft tissue. These values were computed at effective energies of 20 and 22 keV.

This energy range was determined by estimating the effective energy of the source spectrum and applying a margin of $\pm 1$ keV. The effective energy was obtained by computing a weighted average of the spectrum, where the weights accounted for beam-hardening effects due to the presence of 1 mm of graphite in all mask apertures. This yielded an effective energy of approximately 21 keV.

To compute the refractive index parameters, we used the following formulas [32]:

$$\beta \approx \frac{\lambda_{\text{eff}}}{4\pi} \rho \left( \frac{\mu}{\rho} \right)_{\text{mix}}, \qquad \delta \approx \frac{r_e \lambda_{\text{eff}}^2 \rho_e}{2\pi},$$

where $\lambda_{\text{eff}}$ is the effective wavelength, $r_e$ is the classical electron radius, $\rho$ is the material density, $\rho_e$ is the electron density, $N_A$ is Avogadro's number, and $(\mu/\rho)_{\text{mix}}$ is the mass absorption coefficient of the material. The necessary physical parameters for the ground-truth reference values were obtained from the NIST database [32]. Because published values of $\delta$ and $\beta$ for mouse brain at 20–22 keV are scarce, we follow standard pre-clinical practice and use human tissue compositions as surrogates for mouse brain and bone [33]. Using these surrogate compositions, we compute $\delta$ and $\beta$ at 20–22 keV from the same NIST dataset.

The resulting $\delta$ and $\beta$ value ranges are shown in Figs. 3(b) and 3(c) using light and dark green boxes to represent soft tissue (gray/white matter) and cortical bone, respectively.

Within the effective energy range considered, both the EI and LJR methods underestimate the soft-tissue $\delta$ value by approximately 15%, while both correctly estimate $\beta$. Regarding cortical bone, the two methods behave differently: EI retrieves $\delta$ less accurately than LJR, while the opposite trend is observed for $\beta$, where EI outperforms LJR. Due to the large dynamic range of the sample, we present separate visualizations for slice reconstructions of soft and hard tissues, each using an appropriate dynamic range for better comparison. As for the cylindrical phantom, the mouse slices were reconstructed with the pixel size set by the recombined

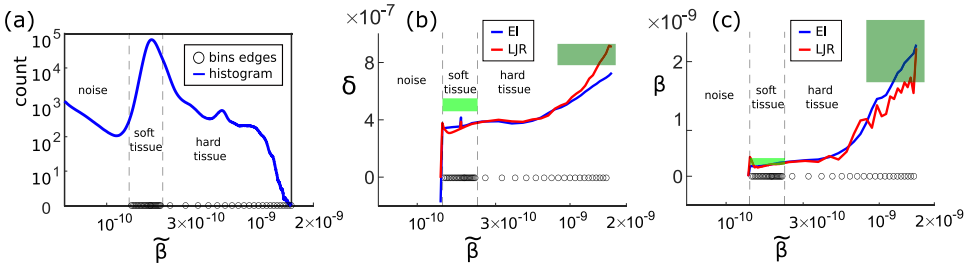


**Fig. 3.** Analysis of the CT reconstruction of the mouse sample dataset, computed using the normalized projection $\mathcal{L}(x_s; t_0)$, where $t_0 = 2$ corresponds to the illumination curve position used for the LJR. (a) 2D histogram (log–log scale) showing the distribution of $\tilde{\beta}$ values across the reconstructed slice. (b) Each point on the red and blue lines corresponds to the mean value of the reconstructed $\delta$ map computed over all pixels within a single bin $B_j$, obtained using the EI and LJR methods, respectively. The points are plotted on a logarithmic scale along the x axis and connected to form the lines. (c) Same as (b), but showing the $\beta$ map instead of the $\delta$ map.

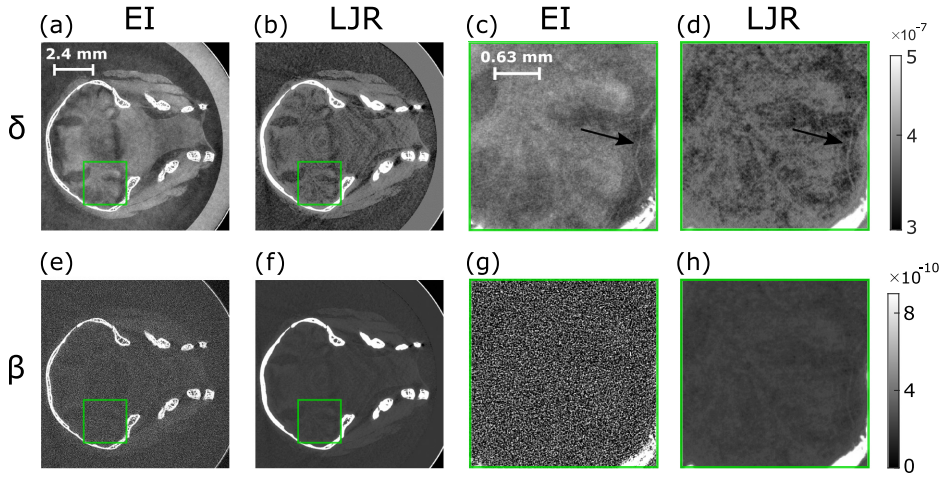


**Fig. 4.** Reconstruction of an intact mouse skull with brain, focusing on soft tissue. The top and bottom rows show the $\delta$-map and $\beta$-map reconstructions, respectively. Panels (c), (d), (g), and (h) display zoomed-in regions corresponding to the green boxes in panels (a), (b), (e), and (f), respectively. The black arrows in (c) and (d) indicate a thin, elongated structure within the brain that is consistently visible across both the LJR and EI reconstructions. While its exact nature is uncertain, its appearance strongly suggests a blood vessel.

eight-dither projections $\frac{\mathcal{P}_1}{8} \approx 9.8$ µm. The slices shown in the first and second columns of Figs. 4 and 5 correspond to cropped regions of the original reconstructions centered on the object, resulting in final displayed images of $1101 \times 1101$ pixels.

### 2. Soft Tissue Visualization

In Fig. 4, we compare the EI and LJR methods, focusing on the soft tissue within the sample.

The top row shows the $\delta$ maps. The contrast between bone and soft tissue is higher in the LJR (b) reconstruction compared to EI (a), and the values are closer to the expected values, which indicates better separation of materials for LJR. However, the zoomed-in views (c) and (d), corresponding to the green boxes in (a) and (b), suggest that LJR produces sharper images compared to EI, potentially revealing more structural detail at soft tissue interfaces. Both methods successfully reconstruct fine features, such as the thin filament highlighted by the black arrows in panels (c) and (d).

The bottom row shows the $\beta$ maps. The EI result (e) appears considerably noisier than the LJR counterpart (f), as more clearly seen in the zoomed-in views (g) and (h), respectively. Although it is well established in the literature that EI-based $\beta$ reconstructions are significantly noisier than their $\delta$-map counterparts, the LJR method appears to yield similar image quality for both contrast channels, which is a new result. Notably, in panel (h), part of the brain remains visible—a result that is highly unexpected in EI $\beta$ maps. This finding is particularly significant: to our knowledge, brain detail visualization in intact skulls has only recently been demonstrated, and only through EI with five illumination curve positions [31] using $\delta$ maps.

### 3. Hard Tissue Visualization

In this section, we revisit the reconstructions presented in the previous section but using a different dynamic range to better visualize hard tissue structures (see Fig. 5). In this case, the image quality of the EI and LJR reconstructions is more similar than in

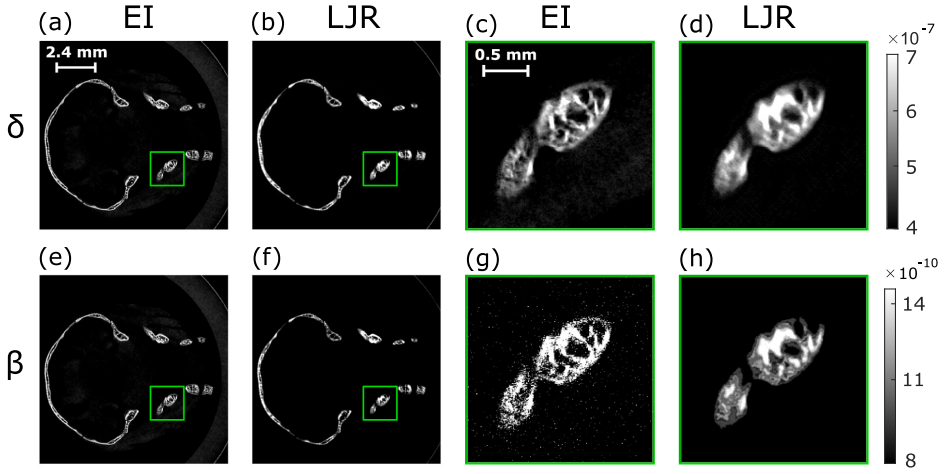


**Fig. 5.** Reconstruction of an intact mouse skull with brain, focusing on hard tissue (analogous to the analysis shown in Fig. 4). The top and bottom rows display the reconstructed $\delta$ maps and $\beta$ maps, respectively. Panels (c), (d), (g), and (h) show zoomed-in views corresponding to the green boxes highlighted in panels (a), (b), (e), and (f), respectively.

Fig. 4. However, some differences become more evident in the zoomed-in views. In particular, the EI $\delta$-map bones shown in panel (c) show finer bone details compared to the LJR result in panel (d), which exhibits a smoother appearance with fewer local intensity variations. A similar pattern is observed in the zoomed-in $\beta$ map. However, as with the soft tissue case, the EI $\beta$-map reconstruction shown in panel (g) is considerably noisier than the corresponding LJR result in panel (h).

Additionally, to further compare the two methods, we computed the CNR at each pixel of each retrieved slice using a $5 \times 5$ pixel kernel. Averaging the resulting CNR values across all pixels of each slice, we obtained average $\delta$ CNRs of 17.5 and 26.1 for the EI and LJR reconstructions, respectively. For $\beta$, the average CNRs were 0.7 for EI and 10.7 for LJR. These results are consistent with the visual impression provided by the images in Fig. 4, where the EI $\beta$ map shows poor quality, while the LJR $\beta$ map demonstrates significantly better performance. Overall, both methods yield higher CNR and improved image quality in the $\delta$ reconstructions compared to the $\beta$ ones. The successful reconstruction of the mouse brain and skull using our method highlights its robustness under challenging imaging conditions. This complex example demonstrates that the LJR model can effectively handle large, multi-scale variations in absorption and phase across the multi-material objects of interest. Additional JR reconstructions for this dataset, including both soft- and hard-tissue visualizations, are provided and discussed in Section 6 of Supplement 1.

#### 4. Computational Time

In this section, we discuss the computational time required to perform the CT reconstruction of the mouse sample. Computations were carried out using a computer with an NVIDIA A6000 48 GB GPU and two CPU AMD EPYC 7453 with 28 cores.

One of the key advantages of the proposed method is the significant reduction in computational time for reconstruction. Retrieving $\delta$ and $\beta$ using the conventional EI method requires Gaussian fitting of the illumination curve for every detector pixel in the analyzed slice, across 2000 projection angles and eight dithering steps, resulting in a total computation time of approximately 30 min. In contrast, the LJR algorithm required approximately 5 min to process the same single slice, with the majority of the time spent computing the *forward* projections (ASTRA Toolbox) needed to generate the thickness functions $T_j$ from the binary masks $B_j$. It is also worth noting that the single-shot approach significantly reduces acquisition time, approximately in proportion to the number of mask positions avoided. In our experiments, using a single mask position instead of five per projection angle resulted in a fivefold reduction in acquisition time and a fivefold reduction in radiation dose to the sample, assuming equal exposure per image.

## 4. SIMULATION: ANALYSIS OF ROBUSTNESS OF THE LJR METHOD

In this section, we evaluate how the LJR reconstruction method is influenced by noise, scattering, mask motion, and the selected point on the IC. The analysis is performed using the EI simulator presented in Section 3.A, employing the same detector pixel size, magnification settings, and spectral profile. The energy spectrum is discretized into four levels at 21, 26, 31, and 36 keV. Simulations also include the EI and SS-EI reconstructions for comparison, with the illumination curve sampled at five positions corresponding to 14%, 58%, 100%, 58%, and 14% of its maximum, which is the same set of IC points used for the post-mortem mouse dataset analyzed in Section 3.D. To approximate a realistic acquisition scenario, we simulated 2000 projections over a full rotation from 0 to 360 deg. The simulated sample consisted of 15 concentric circular rings centered at the origin of the $(x, z)$ plane. The radii increased uniformly from 0.5 to 10 mm. For each ring and for each energy level, a distinct pair of $\delta$ and $\beta$ was assigned. To generate a challenging simulation for the LJR method, with a wide range of $\gamma = \delta/\beta$ values, $\delta$ was increased linearly from the inner to the outer ring while $\beta$ was decreased. Accordingly, $\delta_{\text{eff}}$ ranged from $2 \times 10^{-7}$ to $9.8 \times 10^{-7}$, while $\beta_{\text{eff}}$ decreased from $13.9 \times 10^{-10}$ to $1 \times 10^{-10}$. To set a realistic energy dependence, the outer ring was initialized using the spectral values of PTFE, independently rescaled to match $\delta_{\text{eff}} = 9.8 \times 10^{-7}$ and $\beta_{\text{eff}} = 1 \times 10^{-10}$. The inner rings were then generated by incrementally decreasing $\delta$ and increasing $\beta$, with a constant step size, until reaching $\delta_{\text{eff}} = 2 \times 10^{-7}$ and $\beta_{\text{eff}} = 13.9 \times 10^{-10}$. This configuration spans a broad range of material properties, with $143 \leq \gamma \leq 9800$ [see Figs. 6(a1) and 6(a2)].

Once the refractive indices for the 15 materials were defined, we simulated the four monochromatic components of each projection separately. After adding noise and scattering, these components were combined using a weighted sum to obtain the corresponding polychromatic projections. To mimic realistic acquisition conditions, Poisson noise was added assuming four noise levels, corresponding to total photon counts of 1000, 3000, 7000, and 10,000 per pixel. These photons were distributed across the four energy bins according to the spectral weights. Scattering was simulated by applying a Gaussian blurring to the illumination curve. Five scattering levels were considered, 0, 100, 200, 300, and 400 $\mu\text{rad}^2$, with the largest value representing highly scattering materials. To assess the robustness of the LJR method with respect to the choice of the IC sampling point, the reconstruction was performed 28 times while varying the selected IC point from 40% to 80% of its maximum. Each simulation scenario was reconstructed three times: once when $P_s$ and $P_f$ were measured at the same point on the illumination curve, and twice more when $P_s$ was acquired at points shifted by 0.3 and 0.6 μm relative to $P_f$. These shifts correspond to approximately 3.5% and 7% of the spacing between adjacent IC sampling points in this setup. To assess the feasibility of an automated setup of the algorithm, minimizing the number of user-defined parameters, *all* simulations in this section were run using the same LJR reconstruction settings. In particular, we set the parameter defined in Section 3.D, as $\Delta\tilde{\beta} = 5 \times 10^{-12}$, $\tilde{\beta}_{\text{ns}} = 2\sigma_+$, with boolean matrices $B_j$ acceptance criterion requiring at least one $5 \times 5$ pixel window containing at least 19 ones. Segmentation was facilitated by adding the same 40% low-pass filter to $\mathcal{L}$ described in Section 3.D. The parameter $\gamma$ was selected as $\gamma = \frac{7\times10^{-7}}{3\times10^{-10}}$. From the analysis of the simulation results, we conclude that both EI and LJR are robust to noise, scattering, and mask misalignment.

SS-EI provides reconstructions with a quality comparable to EI and LJR only for the $\beta$ maps, whereas the corresponding $\delta$ maps are largely inaccurate. This mismatch between the SS-EI $\delta$- and $\beta$-map reconstructions is due to the constant $\gamma = \delta/\beta$ assumption. Under this assumption, the normalized projection used by SS-EI is mainly driven by the $\beta$ contribution, since in Eq. (2) the negative exponential term associated with absorption has, on average, a stronger effect than the $\delta$-dependent illumination curve

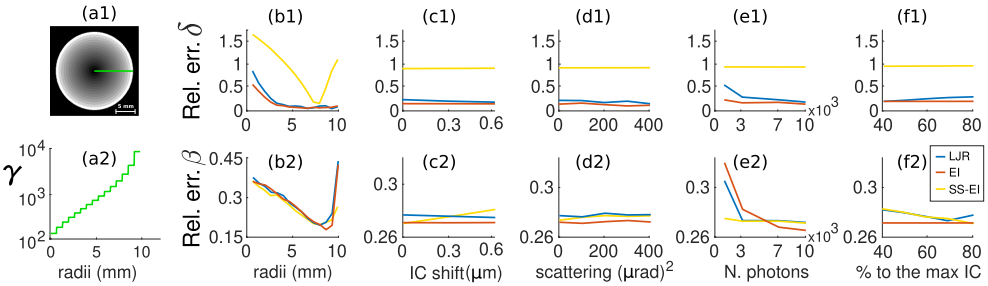


**Fig. 6.** Simulations of CT reconstruction of a multi-material phantom composed of 15 concentric rings. Panel (a1) shows the ground-truth map of $\gamma_{\text{eff}} = \frac{\delta_{\text{eff}}}{\beta_{\text{eff}}}$ in the $(x, z)$ plane on a log scale. Panel (a2) represents the green line plot in panel (a1). Plots in (b1) and (b2) report the relative reconstruction errors $\mathcal{E}$ for EI, LJR, and SS-EI as a function of the materials, with each point corresponding to one of the 15 materials. Panels (c1) and (c2) display the slice-wise errors for mask misalignments of 0, 0.3, and 0.6 μm. Panels (d1) and (d2) show the errors obtained for scattering levels of 0, 100, 200, 300, and 400 μrad$^2$. Panels (e1) and (e2) report the errors for Poisson noise levels corresponding to 1000, 3000, 7000, and 10,000 photons per pixel. Panels (f1) and (f2) show the reconstruction errors obtained with LJR and SS-EI when varying the single IC sampling point between 40% and 80% of its maximum, compared against EI reconstructed with default parameters.

shift. Consequently, when the true $\gamma$ varies substantially across the sample, the absorption reconstruction can remain reasonably reliable, while the phase reconstruction becomes inaccurate. LJR also shows robustness with respect to the choice of the IC sampling point, although the reconstruction error is smallest when the IC point lies between 40% and 60% of its maximum. As expected, LJR is slightly more sensitive to noise and scattering than EI since it relies on fewer measurements to perform the retrieval.

Additional supporting plots are provided in Section 3 of Supplement 1. Representative results are shown in Fig. 6, where each panel varies a single parameter, while the others are kept fixed. The default simulation settings are 7000 photons per pixel, a mask misalignment of 0.3 μm, a scattering level of 100 μrad$^2$, and a single-shot IC sampling point at 65% of the IC maximum. In all panels of Fig. 6 except (a1) and (a2), we report the relative error $\mathcal{E}$ between the EI, LJR, or SS-EI reconstructions and the ground-truth slices defined by $\delta_{\text{eff}}(x, z)$ and $\beta_{\text{eff}}(x, z)$. The error metric is given by $\mathcal{E}(A, B) = 2\frac{||A-B||}{||A||+||B||}$, where $||A|| := (\sum_{i,j} A_{ij}^2)^{1/2}$. Overall, for both EI and LJR, the error in the $\beta$ reconstructions is higher than that in the $\delta$ reconstructions, yet it is more consistent across the varied conditions. This behavior is mainly due to the systematic bias introduced by beam hardening, which prevents exact retrieval of $\beta$, and to the challenging nature of the simulated sample, which spans a large range of $\beta$ and $\delta$ values varying in opposite directions.

### A. Final Considerations

The LJR method achieved qualitatively and quantitatively good results comparable to those of EI. As expected for a single-shot approach, it can be more prone to noise than EI, which exploits multiple acquisitions; however, it does not require fitting steps, which can themselves introduce additional sources of error. A natural extension of this work is the implementation of LJR in full 3D, which may further improve robustness by enabling more consistent segmentation across adjacent slices.

## 5. CONCLUSION

We have introduced a novel LJR method for edge illumination X-ray phase-contrast imaging that significantly improves upon existing JR approaches in both efficiency and robustness, given the inherent convex nature of the method. By leveraging a first-order Taylor expansion of the logarithm of the normalized raw projections, we reformulated the EI forward model into a linear, convex problem—eliminating local minima and reducing computational cost. The proposed method does not require prior assumptions about the sample composition or Gaussian fitting of the illumination curve, making it broadly applicable and straightforward to implement. We showed the validity of the proposed method with both simulated and experimental data. In particular, in both multi-material rod phantom simulation and experimental, LJR nearly perfectly matched conventional multi-exposure EI results.

In the most demanding test, an intact mouse skull with soft brain tissue, LJR robustly recovered detailed soft-tissue interfaces and high-contrast bone structures with only a single mask position per angle (Figs. 4 and 5), a capability previously unattained in lab-based EI systems. LJR achieved slice reconstructions in $\approx 5$ min, with the majority of the time spent on the segmentation task (versus $\approx 30$ min for conventional EI) owing to its linearized single-shot formulation. By eliminating the need for multiple exposures per view, LJR sidesteps the "prolonged data acquisition times" of EI systems. Importantly, LJR produces quantitative, high-fidelity reconstructions of both phase ($\delta$) and absorption ($\beta$) contrasts, even in highly challenging, multi-material specimens. For example, we successfully recovered detailed soft-tissue contrast of an intact mouse brain inside its skull, demonstrating that LJR yields accurate image quality and quantitative accuracy for such complex samples. Conventional JR approaches are iterative and computationally expensive, and to our knowledge, they have rarely been validated on thick, heterogeneous samples. In contrast, LJR's fast semi-analytical and linear solver proved robust and reliable under these difficult conditions. The LJR workflow relies on a preliminary material segmentation to guide the reconstruction. Once the parameters are set, this segmentation is performed automatically; in Section 4, we proposed a standard parameter setting that is applicable to generic multimaterial samples.

Overall, by reducing reconstruction times by orders of magnitude while maintaining quantitative accuracy, LJR lays the foundation for accelerated single-shot multi-material phase-contrast imaging. This capability is especially promising for biomedical applications—where X-ray phase-contrast tomography can provide better differentiation of soft tissues—and also for high-throughput studies in materials science and other fields. In

summary, LJR significantly advances the practicality of quantitative edge-illumination X-ray imaging by enabling fast, reliable single-shot reconstructions across a wide range of challenging specimens.

**Funding.** Engineering and Physical Sciences Research Council (EP/X018377/1, EP/W008092/1, EP/R513143/1 –2592407, EP/T517793/1–2592407); Royal Academy of Engineering (CiET1819/2/78); Research Foundation - Flanders (S003421N).

**Disclosures.** The authors declare no conflicts of interest.

**Data availability.** The code implementing the proposed algorithm will be made available by the corresponding author upon reasonable request.

**Supplemental document.** See Supplement 1 for supporting content.

## REFERENCES

1. A. Olivo, K. Ignatyev, P. R. Munro, *et al.*, "Design and realization of a coded-aperture based X-ray phase contrast imaging for homeland security applications," Nucl. Instrum. Methods Phys. Res. Sect. A Accel. Spectrom. Detect. Assoc. Equip. **610**, 604–614 (2009).
2. A. Olivo, S. Gkoumas, M. Endrizzi, *et al.*, "Low-dose phase contrast mammography with conventional x-ray sources," Med. Phys. **40**, 090701 (2013).
3. L. Massimi, T. Suaris, C. K. Hagen, *et al.*, "Volumetric high-resolution X-ray phase-contrast virtual histology of breast specimens with a compact laboratory system," IEEE Trans. Med. Imaging **41**, 1188–1195 (2022).
4. F. Arfelli, M. Assante, V. Bonvicini, *et al.*, "Low-dose phase contrast x-ray medical imaging," Phys. Med. Biol. **43**, 2845–2852 (1998).
5. R. A. Lewis, "Medical phase contrast x-ray imaging: current status and future prospects," Phys. Med. Biol. **49**, 3573–3583 (2004).
6. T. Donath, F. Pfeiffer, O. Bunk, *et al.*, "Toward clinical X-ray phase-contrast CT: demonstration of enhanced soft-tissue contrast in human specimen," Investig. Radiol. **45**, 445–452 (2010).
7. S. C. Mayo, A. W. Stevenson, and S. W. Wilkins, "In-line phase-contrast X-ray imaging and tomography for materials science," Materials **5**, 937–965 (2012).
8. J. Moosmann, A. Ershov, V. Altapova, *et al.*, "X-ray phase-contrast in vivo microtomography probes new aspects of Xenopus gastrulation," Nature **497**, 374–377 (2013).
9. A. Olivo, F. Arfelli, G. Cantatore, *et al.*, "An innovative digital imaging set-up allowing a low-dose approach to phase contrast applications in the medical field," Med. Phys. **28**, 1610–1619 (2001).
10. A. Olivo, S. Pani, D. Dreossi, *et al.*, "A multilayer edge-on single photon counting silicon microstrip detector for innovative imaging techniques in diagnostic radiology," Rev. Sci. Instrum. **74**, 3460–3465 (2003).
11. A. Olivo, "Edge-illumination x-ray phase-contrast imaging," J. Phys. Condens. Matter **33**, 363002 (2021).
12. M. Endrizzi, P. C. Diemoz, T. P. Millard, *et al.*, "Hard X-ray dark-field imaging with incoherent sample illumination," Appl. Phys. Lett. **104**, 024106 (2014).
13. L. Massimi, T. Partridge, A. Astolfo, *et al.*, "Optimization of multipoint phase retrieval in edge illumination X-ray imaging: a theoretical and experimental analysis," Med. Phys. **48**, 5884–5896 (2021).
14. P. C. Diemoz, F. A. Vittoria, C. K. Hagen, *et al.*, "Single-image phase retrieval using an edge illumination X-ray phase-contrast imaging setup," J. Synchrotron. Radiat. **22**, 1072–1077 (2015).
15. P. C. Diemoz, C. K. Hagen, M. Endrizzi, *et al.*, "Single-shot X-ray phase-contrast computed tomography with nonmicrofocal laboratory sources," Phys. Rev. Appl. **7**, 044029 (2017).
16. D. Paganin, S. C. Mayo, T. E. Gureyev, *et al.*, "Simultaneous phase and amplitude extraction from a single defocused image of a homogeneous object," J. Microsc. **206**, 33–40 (2002).
17. A. Zamir, P. C. Diemoz, F. A. Vittoria, *et al.*, "Edge illumination X-ray phase tomography of multi-material samples using a single-image phase retrieval algorithm," Opt. Express **25**, 11984–11996 (2017).
18. M. Beltran, D. Paganin, K. Uesugi, *et al.*, "2D and 3D X-ray phase retrieval of multi-material objects using a single defocus distance," Opt. Express **18**, 6423–6436 (2010).
19. M. A. Beltran, D. M. Paganin, K. K. Siu, *et al.*, "Interface-specific x-ray phase retrieval tomography of complex biological organs," Phys. Med. Biol. **56**, 7353–7369 (2011).
20. S. Maretzke, "A uniqueness result for propagation-based phase contrast imaging from a single measurement," Inverse Probl. **31**, 065003 (2015).
21. S. Maretzke, M. Bartels, M. Krenkel, *et al.*, "Regularized Newton methods for x-ray phase contrast and general imaging problems," Opt. Express **24**, 6490–6506 (2016).
22. M. V. Teuffenbach, T. Koehler, A. Fehringer, *et al.*, "Grating-based phase-contrast and dark-field computed tomography: a single-shot method," Sci. Rep. **7**, 7476 (2017).
23. Y. Chen, H. Guan, C. K. Hagen, *et al.*, "Single-shot edge illumination x-ray phase-contrast tomography enabled by joint image reconstruction," Opt. Lett. **42**, 619–622 (2017).
24. P. Modregger, J. Meganck, C. K. Hagen, *et al.*, "Improved iterative tomographic reconstruction for X-ray imaging with edge-illumination," Phys. Med. Biol. **64**, 205008 (2019).
25. N. Six, J. Renders, J. De Beenhouwer, *et al.*, "Joint multi-contrast CT for edge illumination X-ray phase contrast imaging using split Barzilai-Borwein steps," Opt. Express **32**, 1135–1150 (2024).
26. Y. Chen and M. A. Anastasio, "Properties of a joint reconstruction method for edge-illumination X-ray phase-contrast tomography," Sens. Imaging **19**, 7 (2018).
27. F. A. Vittoria, M. Endrizzi, P. C. Diemoz, *et al.*, "X-ray absorption, phase and dark-field tomography through a beam tracking approach," Sci. Rep. **5**, 16318 (2015).
28. C. K. Hagen, M. Endrizzi, P. C. Diemoz, *et al.*, "Reverse projection retrieval in edge illumination x-ray phase contrast computed tomography," J. Phys. D Appl. Phys. **49**, 255501 (2016).
29. P. R. Munro and A. Olivo, "X-ray phase-contrast imaging with polychromatic sources and the concept of effective energy," Phys. Rev. A At. Mol. Opt. Phys. **87**, 053838 (2013).
30. F. A. Vittoria, P. C. Diemoz, M. Endrizzi, *et al.*, "Strategies for efficient and fast wave optics simulation of coded-aperture and other x-ray phase-contrast imaging methods," Appl. Opt. **52**, 6940–6947 (2013).
31. A. Mazzolani, A. Astolfo, I. Buchanan, *et al.*, "Accurate and noise robust crosstalk removal techniques for edge illumination phase-based x-ray imaging systems," Opt. Express **33**, 16187–16201 (2025).
32. J. Hubbell and S. Seltzer, *NIST: X-Ray Mass Attenuation Coefficients* (2004).
33. A. Vaniqui, L. E. Schyns, I. P. Almeida, *et al.*, "The impact of dual energy CT imaging on dose calculations for pre-clinical studies," Radiat. Oncol. **12**, 181 (2017).